Journal of Materials Chemistry C

ROYAL SOCIETY OF CHEMISTRY

PAPER

Cite this: *J. Mater. Chem. C*, 2024, **12**, 562

Interface passivation with $Ti_3C_2T_x$-MXene doped PMMA film for highly efficient and stable inverted perovskite solar cells†

João Pedro F. Assunção,[a] Hugo G. Lemos,*[a] Jéssica H. H. Rossato,[a] Gabriel L. Nogueira,[a] João V. M. Lima,[a] Silvia L. Fernandes,[b] Rafael K. Nishihora,[c] Ricardo V. Fernandes,[d] Sidney A. Lourenço,[d] Diego Bagnis,[b] Sydney F. Santos[c] and Carlos F. O. Graeff*[a]

Received 18th October 2023,
Accepted 28th November 2023

DOI: 10.1039/d3tc03810f

rsc.li/materials-c

Achieving inverted perovskite solar cells (PSCs) that combine high efficiency and long-term stability is still challenging due to intrinsic material issues and low tolerance to environmental factors. The use of an ultra-thin poly(methyl methacrylate) (PMMA) layer to passivate interfacial defects as well as working as a physical barrier to extrinsic factors is promising. However, the low electrical conductivity of PMMA may have deleterious effects on charge extraction. Herein, we explored the use of $Ti_3C_2T_x$ MXene as a PMMA additive (PMMA:MX) to tune the electrical features of the passivation layers. The optimal concentration of MXenes resulted in improvement of the PSC photovoltaic parameters, boosting their efficiency to 21.30 ± 0.51% (22.1% for the benchmark PSC). Electrical characterizations indicate a reduction of trap state densities accompanied by mitigation of non-radiative recombination. These features contributed to an increase in the extraction of photo-generated carriers and a considerable enhancement of V_{oc}. The improved performance may be attributed to the electrical properties of MXenes and the better wettability of the PMMA:MX interface. Furthermore, the combination of hydrophobic characteristics and passivation features of the PMMA:MX layer resulted in more stable PSCs. The PMMA:MX based devices maintained 95% of their original PCE after 3000 h (ISOS-D-1I) and took 3× longer to reach T80 compared to the control PSC under heat and light soaking (ISOS-L-2).

Introduction

Perovskite solar cells (PSCs) have attracted widespread attention in academia and industry due to their high-power conversion efficiency (PCE) and potential for low-cost, sustainable, and large-scale manufacturing. Since their first appearance in 2009, the PCE of PSCs has rapidly increased from 3.8% to over 26%, making them a strong candidate to replace silicon solar cells in practical applications.[1] In particular, the planar inverted architecture (p–i–n) shows good compatibility with flexible substrates and the possibility for integrating these devices with silicon or tandem solar cells.[2,3] In addition, inverted PSCs usually show reduced hysteresis and better environmental stability when compared to the regular architecture due to the presence of a high electrical conductive, hydrophobic and additive-free PCBM rear layer.[3]

Despite the outstanding advantages of PSCs, achieving large-scale inverted devices that combine high efficiency and long-term stability remains a challenge. This is due to several intrinsic unresolved issues related to the perovskite and charge transport materials. Among them, interfacial and bulk defects in addition to poor energy-level alignment between perovskite/charge transport layers result in recombination losses, which compromises charge extraction.[2,4] These non-radiative recombination processes also affect the solar cell V_{oc} and FF. Moreover, ion diffusion across the layers promotes charge accumulation at interfaces, affecting the operation and stability of PSCs.[5] Thus, interfacial engineering strategies to mitigate ion diffusion and defect density improve both device efficiency and stability[2,3,6]

The addition of a passivation layer between the perovskite and the charge transport layers is an interesting interfacial

[a] *São Paulo State University (UNESP), School of Sciences, Department of Physics, Bauru, SP, 17033-360, Brazil. E-mail: hugo.lemos@unesp.br, carlos.graeff@unesp.br*
[b] *Oninn – Innovation Center, Belo Horizonte, MG, 31035-536, Brazil*
[c] *Federal University of ABC (UFABC), Center for Engineering, Modeling and Applied Social Science, Santo André, SP, 09210-580, Brazil*
[d] *Materials Science and Engineering Program (PPGCEM), Federal Technological University of Paraná (UTFPR), Londrina, PR, Brazil*

† Electronic supplementary information (ESI) available. See DOI: https://doi.org/10.1039/d3tc03810f

engineering approach.[7–11] For instance, Wang *et al.*[12] studied the introduction of thin polymeric insulating films, such as polystyrene (PS), Teflon and polyvinylidene-trifluoroethylene (PVDF-TrFE), between the perovskite and the electron transport layer (ETL). The insulating polymeric layer enhanced stability against humidity for non-encapsulated PSCs. In addition, the passivation layer blocked the photogenerated holes, while promoting the transport of the photogenerated electrons by tunneling.[12]

Similarly, thin passivation layers of poly(methyl methacrylate) (PMMA) have been shown to reduce trap density and to improve the PCE of devices either deposited before or after the perovskite layer.[7,13–15] Yang *et al.*[7] used PMMA as an interlayer between the perovskite and Spiro-OMeTAD. This study shows that PMMA layer thickness and the conductivity are highly dependent on the solution concentration, once higher concentrations led to a higher film thickness negatively impacting the device series resistance (R_s). Under optimal conditions, they improved the solar cell PCE by passivating surface defects of the perovskite layer as well as filling pinholes and grain boundaries, and thus reducing carrier recombination losses. Moreover, the PMMA film protected the perovskite from direct contact to the atmosphere resulting in better device stability.[7] Peng *et al.*[14] reported the application of a PMMA film at both perovskite/ETL and perovskite/HTL interfaces. Spectroscopic and numerical analyses revealed that the carbonyl groups (C═O) from PMMA passivates Pb^{2+} ions *via* Lewis base electronic interaction.[14] Thus, the reduced number of traps states associated with uncoordinated Pb atoms mitigates nonradiative recombination. However, due to the high resistivity of PMMA, charge transport is limited, reducing the charge extraction of the devices. To improve charge transport, high conducting materials such as PCBM have been incorporated into PMMA.[16–18] Peng *et al.*[18] successfully increased the conductivity of the PMMA passivation layer by incorporating PCBM. The author showed that an ultra-thin layer based on a PMMA:PCBM blend effectively passivated the perovskite/m-TiO_2 interface leading to a reduction in recombination and hysteresis and maximized efficiency.[18]

MXene is an emerging class of two-dimensional materials with a general chemical formula of $M_{n+1}X_nT_x$, where M refers to an early transition metal, X represents carbon or/and nitrogen, and T_x stands for the functional groups (such as F, O, and OH). This material shows unique chemical and physical properties such as high electrical conductivity, high transmittance and good thermal stability.[19] Additionally, functional groups can modify their work function depending on type and concentration.[20,21] Therefore, MXenes present tunable energy levels, making them promising materials for applications in organic,[22] dye-sensitized[23] and perovskite[24] based solar cells. Recently, several studies have reported the use of $Ti_3C_2T_x$ MXenes as an additive in the perovskite active layer,[25,26] ETLs[25,27,28] and HTLs.[22] Other studies have explored the use of MXenes as passivating layers.[29,30] These studies showed that the addition of MXenes in PSCs improve their efficiency and stability due to improved conductivity and reduced charge recombination.

Notwithstanding the recent advances in passivation strategies of PSCs *via* thin polymeric layers, their use in inverted devices is still to be further explored. All the aforementioned studies used passivation layers under or onto perovskite layers in a regular n–i–p architecture. As mentioned previously, the p–i–n architecture is compatible with large-scale, efficient and stable devices. In addition, MXenes demonstrate excellent bonding with polymeric matrices, maintaining their electronic properties, which make them attractive for enhancing the electrical conductivity of polymers.[31] In this context, we explored the incorporation of $Ti_3C_2T_x$ MXene into PMMA (PMMA:MX) as an efficient passivation layer in p–i–n PSCs. The PMMA:MX passivation layer provided a promising interface between the perovskite and ETL, reflected in an improved charge mobility and density of extracted charges. The improved performance could be attributed to the improved wettability between the perovskite/ETL, high electrical conductivity of the $Ti_3C_2T_x$, and defect passivation. The use of the PMMA:MX passivation layer also considerably increased the stability of the PSCs under standard degradation protocols (ISOS-L-2).

Experimental

$Ti_3C_2T_x$ MXene preparation

The $Ti_3C_2T_x$ MXene was obtained using the minimally intensive layer delamination (MILD) method.[32] For this, the Ti_3AlC_2 MAX phase (Sigma Aldrich) was exfoliated in a 12 M LiF/9 M HCl solution under continuous stirring for 24 h at room temperature. Then, the solution was washed with high purity water several times by centrifugation at 3500 rpm for 5 min until pH 5 was reached. The MXenes were then vacuum-filtered using a cellulose acetate microfiltration membrane (Analitica, 0.47 μm) and dried in a desiccator at room temperature. Inside an inert atmosphere glovebox, 0.1 mg of MXene was added to 1 mL of anhydrous chlorobenzene (C_6H_5Cl – Sigma Aldrich). Lastly, out of the glovebox, the sealed flask was sonicated in an ultrasound bath (Unique) for 15 min at 25 °C, resulting in a 0.3 mg mL^{-1} MXene concentrated solution.

PMMA:MXene solution preparation

The poly(methyl methacrylate) (PMMA $M_W \sim 120\,000$, Sigma Aldrich) precursor solution was prepared with 1 mg mL^{-1} concentration in anhydrous chlorobenzene (CB). Various solutions were prepared by mixing the MXene and PMMA precursor solutions (0.3, 1.5 and 3% by weight percent of $Ti_3C_2T_x$ with respect to PMMA, named henceforth PMMA:MX). For comparison, a pure PMMA solution was prepared.

Perovskite preparation

A $Cs_{0.17}FA_{0.83}Pb(I_{0.83}Br_{0.17})_3$ double-cation mixed-halide perovskite solution was prepared under an inert atmosphere inside the nitrogen-filled glove box. In this procedure, an iodide-based solution containing 1.2 M lead(II) iodide (PbI_2, TCI Chemicals), 1.0 M formamidinium lead iodide (FAI, Sigma Aldrich) and 0.2 M cesium iodide (CsI, Sigma-Aldrich) in a mixture (4 : 1 v/v)

of anhydrous *N*,*N*-dimethylformamide (DMF, Sigma Aldrich) and anhydrous dimethyl sulfoxide anhydrous (DMSO, Sigma Aldrich) was prepared. Likewise, a bromide-based solution was prepared by dissolving 1.2 M lead(II) bromide ($PbBr_2$, Sigma Aldrich) and 1.2 M formamidinium bromide (FABr, Greatcell-solar) in a mixture (4 : 1 v/v) of DMF/DMSO. The two solutions were stirred overnight at 70 °C and then mixed to obtain a $FAPbBr_3$: $CsFAPbI_3$ (17 : 83% v/v) solution. Before deposition, the solution was filtered with a 0.45 μm syringe filter.

Solar cell fabrication

Fluorine-doped Tin Oxide (FTO) coated glass (7 Ω sq^{-2}, Sigma Aldrich) was patterned using Kapton tape® and etched with Zn powder (Neon, Brazil) and hydrochloric acid (HCl 37%, Neon). The substrates were sequentially cleaned with Extran® solution (50% v/v in H_2O), pure deionized water, acetone, and 2-propanol for 20 min each in an ultrasound bath. After drying with N_2, the substrates were UV-Ozone (Ossila Ltda) cleaned for 15 min. The substrates were then inserted into a nitrogen-filled glove-box for device fabrication. The HTL layer was deposited using a [2-(3,6-dimethoxy-9*H*-carbazol-9-yl)ethyl]phosphon (MeO-2PACz, TCI Chemicals) SAM solution (0.35 mg mL^{-1}) in anhydrous isopropanol by spin coating at 3000 rpm for 30 s. The $Cs_{0.17}FA_{0.83}Pb(I_{0.83}Br_{0.17})_3$ perovskite precursor solution was spin-coated on top of the HTL (1000 rpm for 5 s and 6000 rpm for 25 s) using CB as the anti-solvent after 20 s of spinning. The perovskite was then thermally annealed at 120 °C for 30 min on a hot plate.

The PMMA and PMMA:MX solutions containing different concentrations of MXenes were spin-coated on top of the perovskite layer at 4000 rpm for 60 s and then thermally annealed at 100 °C for 10 min. For the ETL layer, a [6,6]-phenyl-C61-butyric acid methyl ester (PCBM, NanoC) solution in CB (20 mg mL^{-1}) was spin-coated at 1000 rpm for 20 s. Lastly, a 2,9-dimethyl-4,7-diphenyl-1,10-phenanthroline Bathocuproine (BCP, TCI Chemicals) solution (4 mg mL^{-1}) in isopropanol was spin-coated at 4000 rpm for 60 s, with a thermally evaporated Ag layer (80 nm) as the top electrode.

Characterization

X-ray diffraction (XRD) patterns were obtained using a Rigaku D/MAX-2100/PC diffractometer equipped with Cu Kα radiation (λ = 1.54056 Å) over an angular range from 3 to 50° at an angular step of 0.02°. X-ray photoelectron (XPS) spectroscopy was carried out using an X-ray spectrometer Scienta – model Omicron ESCA+, equipped with a monochromator and source Al Kα X-ray excitation ($h\nu$ = 1486.6 eV). The spectra were analysed with the CasaXPS software and Shirley algorithm for spectral background removal. For XPS, the C 1s carbon peak was collected at 284.6 ± 0.1 eV and used as a reference for energy calibration. UV-Vis absorbance spectra of PMMA and PMMA: MXene solutions were measured at a wavelength of 280–1000 nm in a quartz cuvette. The spectra were collected by using a PerkinElmer Lambda 1050 spectrometer. The CB solvent was used as a reference. Morphological analyses were carried out using JMS-6701F JEOL Field Emission Scanning Electron Microscopy (FE SEM). Atomic Force Microscopy (AFM) was performed by using a Park XE7 AFM microscope in non-contact mode in a 5 μm × 5 μm area. External Quantum Efficiency (EQE) measurements were carried out with a PTS-2-QE Quantum Efficiency/IPCE System from Sciencetech. Contact angle measurements were carried using an Ossila Contact Angle Goniometer, with a solution of 20 mg mL^{-1} of PCBM in CB.

Current density *versus* voltage (*J*–*V*) curves of PSCs were measured using a Keithley 2400 source measurement unit under simulated sunlight at AM 1.5G illumination (100 mW cm^2) from a Newport solar simulator (model Class AAA, 94023A-U). The sunlight power was calibrated with a certified silicon solar cell. External Quantum Efficiency (EQE) measurements were carried out using a PTS-2-QE Quantum Efficiency/IPCE System from Sciencetech. Charge extraction in a linearly increased voltage (CELIV), photo-CELIV, transient photovoltage (TPV), transient photocurrent (TPC), electrical impedance spectroscopy (EIS) and dark *J*–*V* curves were recorded in a PAIOS system from Fluxin. Steady-state photoluminescence (PL) was carried out using a 473 nm laser and an USB-4000 mini-spectrometer to detect the fluorescence light. Time-resolved PL (TRPL) spectroscopy was measured using a Fluo Time 200 from PicoQuant with a 470 nm picosecond pulsed diode laser. All the performed measurements consider the laser emission response (IRF) for the decay adjustments. Stability tests were performed following protocols ISOS-D-1I, ISOS-D-1 and ISOS-L-2.[33] The devices were maintained under an inert atmosphere (23 °C) and the photovoltaic performance was evaluated with 1-month intervals for ISOS-D-1I. For ISOS-D-1, the devices were kept under ambient conditions (23 °C and humidity of ~40%) and the photovoltaic performance was monitored periodically. Lastly, encapsulated devices under an ISOS-L-2 protocol were exposed to continuous simulated sunlight at AM 1.5G illumination (100 mW cm^2) at 65 °C, and the photovoltaic performances were evaluated with intervals of 30 min and kept under maximum power point potential.

Results and discussion

Film characterization

Fig. 1 shows a schematic illustration of the MILD method for the exfoliation of Ti_3AlC_2 MAX phase. The successful acid etching of the Al layer from the MAX phase and its exfoliation to $Ti_3C_2T_x$ MXene were confirmed by XRD analysis (Fig. S1, ESI†). The diffractogram of the MAX phase exhibits the characteristic peaks of the lamellar carbide crystalline structure. Notably, the XRD pattern of $Ti_3C_2T_x$ shows fewer and broader peaks indicating a disruption of the crystalline structure after acid etching. In addition, closer inspection of the 2θ position of the (002) plane shows a pronounced shift to lower angles from 9.4° (Ti_3AlC_2) to 6.6° ($Ti_3C_2T_x$), indicating an increase of the planar *d*-spacing due to the presence of functional groups (–O, –OH and –F) and solvated Li^{+1} ions after etching. The presence of these functional groups facilitates MXene dispersion in a variety of protic solvents. Even though CB has a low

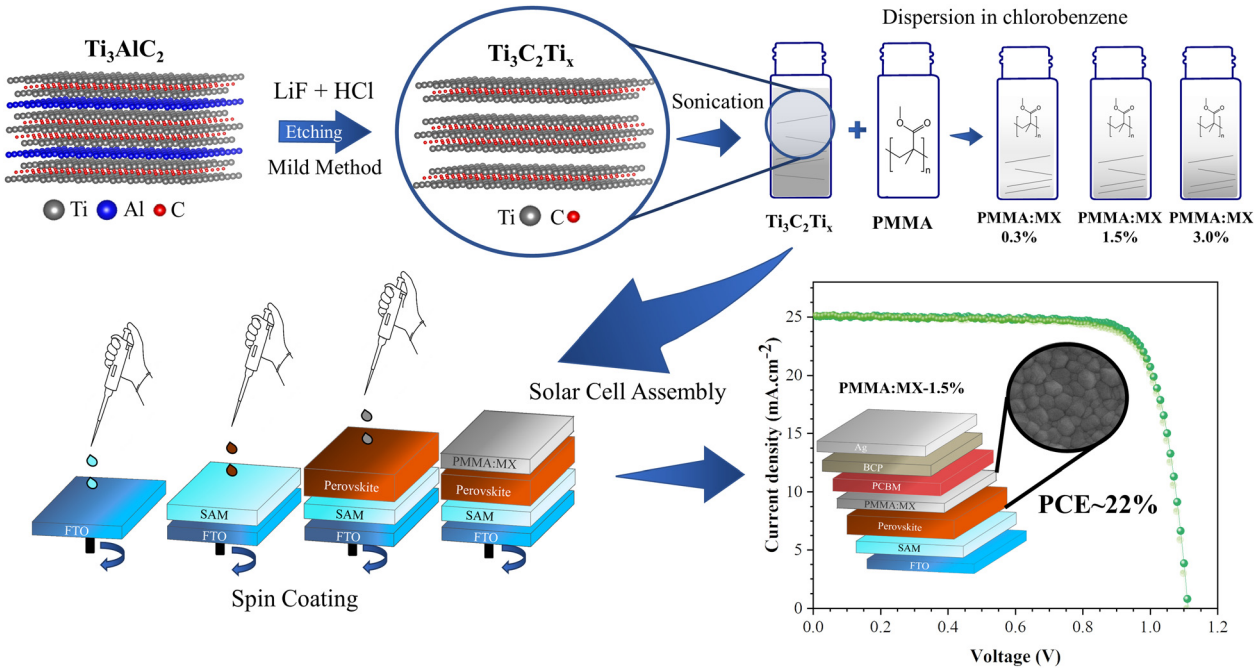

Fig. 1 Schematic illustration of the synthesis of $Ti_3C_2T_x$ MXene and the fabrication of PMMA and PMMA:MX (0.3, 1.5 and 3.0 wt%) based PSCs.

polarity index, the delaminated layers of $Ti_3C_2T_x$ could be dispersed in low concentrations of 0.1 mg ml^{-1}. Then, the 2D material was incorporated in PMMA solutions in different concentrations and applied as a passivation layer in PSCs, as shown in Fig. 1.

The addition of $Ti_3C_2T_x$ MXene into PMMA solutions was assessed by structural and spectroscopy analyses. Fig. 2(a) shows the XRD patterns of pure PMMA, PMMA:MX-3% and pure $Ti_3C_2T_x$ MXene films deposited onto glass. The XRD diffractogram of pure PMMA shows a broad peak at $2\theta \approx 23^\circ$, indicating its amorphous nature. After the addition of MXene into PMMA, a peak at $2\theta \approx 6^\circ$ assigned to the (200) plane of $Ti_3C_2T_x$ was observed. The mixture of MXenes and PMMA was also confirmed by UV-Vis (Fig. 2(b)). The UV-Vis spectrum of $Ti_3C_2T_x$ shows a strong and broad characteristic absorption in the UV region, in addition to a pronounced

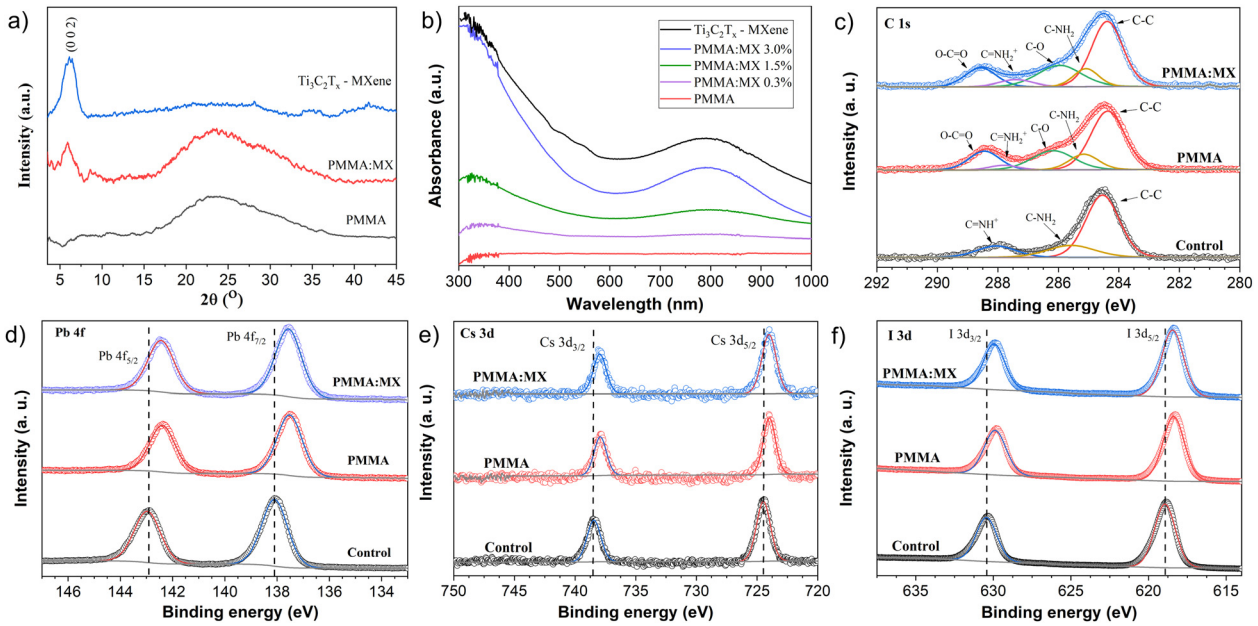

Fig. 2 (a) XRD patterns of pure $Ti_3C_2T_x$ MXene, pure PMMA and PMMA:MX-3.0% films. (b) UV-Vis absorbance spectra of pure $Ti_3C_2Ti_x$ MXene, pure PMMA and PMMA:MX (0.3%, 1.5% and 3.0%) in CB-based solution. High-resolution XPS spectra of (c) C 1s, (d) Pb 4f, (e) Cs 3d and (f) I 3d for perovskite (control) and samples containing the ultrathin PMMA and PMMA:MX-1.5% layers over perovskites, respectively.

localized surface plasmon resonance band at ~800 nm.[34,35] These features were clearly observed in PMMA:MX.

XPS analysis was performed to further investigate the interaction between PMMA and PMMA:MX with $Cs_{0.17}FA_{0.83}Pb(I_{0.83}Br_{0.17})_3$ perovskite. The high-resolution XPS spectra of C 1s (Fig. 2(c)) and N 1s (Fig. S2(b), ESI†) show the characteristic peaks at ≈287.7 and ≈401.7 eV related to C═NH_2^+ of the FA component, respectively.[36] With the addition of the PMMA and PMMA:MX, the peaks related to O–C═O and C–O functional groups are found in C 1s (Fig. 2(c)) and O 1s (Fig. S2(a), ESI†) spectra, indicating the presence of PMMA.[37] In addition, the incorporation of PMMA and PMMA:MX results in a shift of the Pb 4f (Fig. 2(d)), Cs 3d (Fig. 2(e)), I 3d (Fig. 2(f)), and Br 3d (Fig. S2(c), ESI†) doublet peaks towards lower energies. This effect is associated with the oxygen from PMMA carbonyl groups (C═O), which act as a Lewis base (electron donor) interacting with Pb^+, Cs^+ and FA^+ cations of the perovskite structure.[14] These shifts resulted from the chemical interactions of PMMA and PMMA:MX with the perovskite ions.[14,37]

The surface morphology of the perovskite, before and after adding the PMMA and PMMA:MX (0.3, 1.5 and 3.0 wt%) layers were evaluated using FE-SEM images, as shown in Fig. 3(a)–(c) and Fig. S3(a), (b) (ESI†). Perovskite film grown over the HTL exhibits a pinhole free surface with large grain sizes of about 205 ± 9 nm. No modification was observed after the addition of the PMMA and PMMA:MX passivation layers (Fig. 3(b), (c) and Fig S3(a), (b), ESI†). The size distribution of perovskite grains with and without the passivation layers showed no significant differences, once no alteration on perovskite crystallization was expected.

The AFM images are shown in Fig. 3(d)–(f) and Fig. S4(a), (b) (ESI†). No significant changes in the root mean square roughness (RMS) was observed after the addition of PMMA and PMMA:MX-0.3% passivation layers (RMS ≈ 22 nm) (Fig. 3(d), (e) and Fig. S4(a), ESI†). The RMS increased from 22 nm to ≈24 nm and ≈26 nm for PMMA:MX-1.5% and PMMA:MX-3.0%, respectively (Fig. 3(f) and Fig. S4b, ESI†). These results indicate the ultra-thin feature of the PMMA layer, which is strongly influenced by the topographical characteristic of the perovskite layer underneath. The rise in surface roughness may be due to the MXene concentration, otherwise it is related to a possible agglomeration of the 2D material.

The wettability of bare perovskite, PMMA and PMMA:MX films to the ETL precursor solution (PCBM in CB) was assessed using contact angle (CA) measurements (Table S1, ESI†). The bare perovskite films showed a CA of 30.3°, which strongly decreased to values in a range of 11–14° after the addition of the passivation layers. The decrease in CA after the deposition of PMMA and PMMA:MX is due to the hydrophobic nature of the polymer. PMMA is soluble in the apolar CB, and electrostatically anchors the cations present in the perovskite layer.[14] Thus, PMMA and PMMA:MX deposition results in the formation of an ETL layer with better quality, in addition to creating a protection capping layer against external agents.[7] Although MXene has a polar nature, the low quantities of 2D material used in this work had no considerable impact on the wettability of the PMMA films.

PSCs electrical characterization

To investigate the effects of the PMMA and PMMA:MX passivation layers on the device performance, we fabricated PSCs with the architecture FTO/HTL/$Cs_{0.17}FA_{0.83}Pb(I_{0.83}Br_{0.17})$/PMMA:MXene/ETL/Ag, shown in Fig. 1. For comparison, devices without the polymeric layer (control) and containing pure PMMA were also assembled. Fig. 4(a) shows the best photovoltaic performance evaluated in reverse scan *J–V* curves under one sun

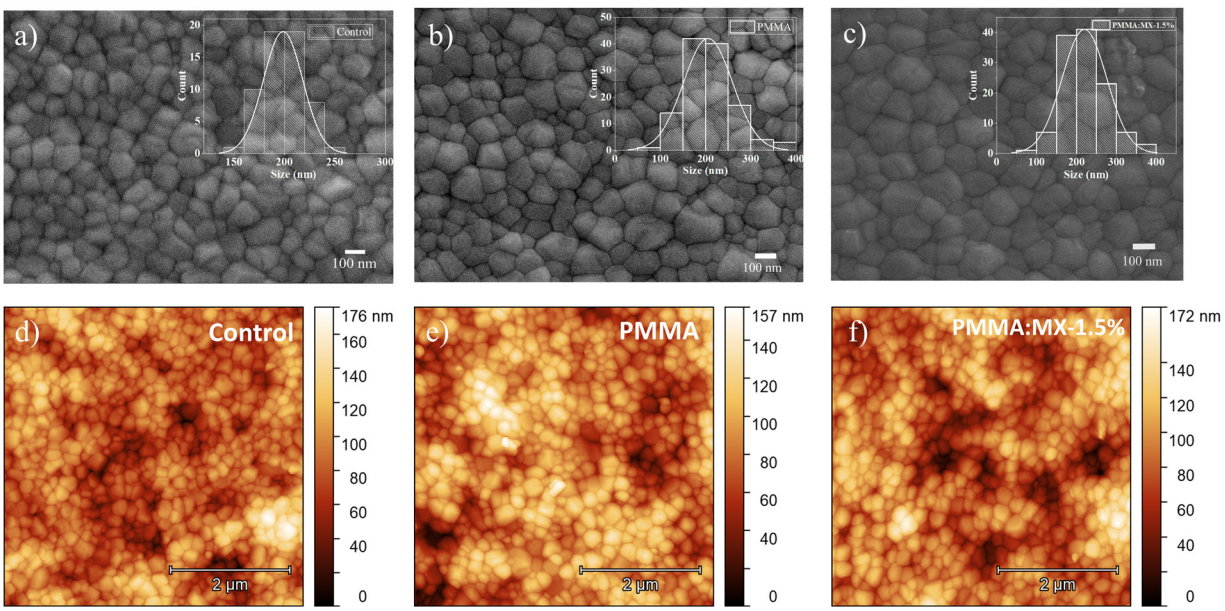

Fig. 3 (a) FE-SEM images and grain size distributions of bare perovskite (a); and perovskite films containing PMMA (b) and PMMA:MX-1.5% (c) passivation layers. AFM images of bare perovskite (d); and perovskite films containing PMMA (e) PMMA and PMMA:MX-1.5% (f) passivation films.

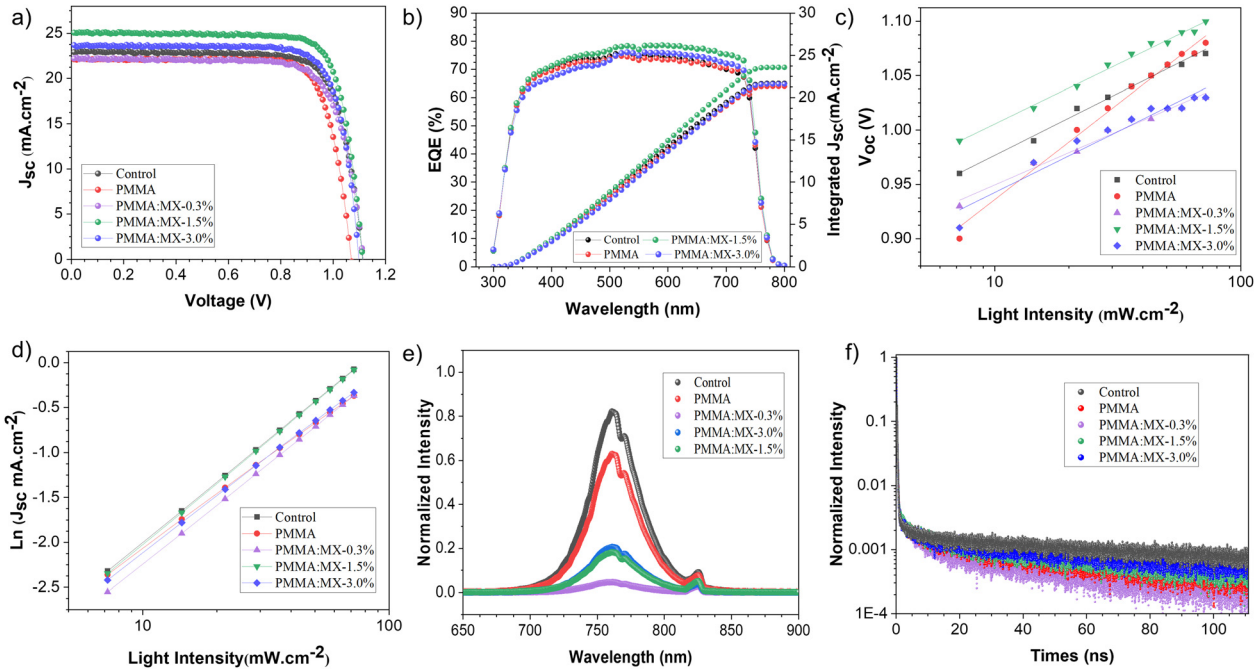

Fig. 4 (a) Current density *versus* voltage ($J \times V$) of the control, PMMA and PMMA:MX (0.3, 1.5 and 3%) best PCSs. (b) EQE and integral current densities of the control, PMMA, PMMA:MX-1.5% and PMMA:MX-3% devices. Irradiation intensity dependent open-circuit potential V_{oc} (c) and short-circuit current J_{sc} (d) of the control, PMMA and PMMA:MX (0.3, 1.5 and 3.0%) PCSs. (e) PL and (f) TRPL of perovskite/PMMA:MX/PCBM.

illumination (AM 1.5G, 100 mW cm^{-2}). Table 1 summarizes the photovoltaic parameters. The small standard deviation reflects the good device reproducibility as observed from the box plot in Fig. S5 (ESI†).

The pure PMMA passivation layer slightly decreased the cell performance. Deleterious effects were mainly observed for J_{sc} and V_{oc}, leading to a poor PCE of 17.78 ± 0.81% when compared to the device without PMMA (19.16 ± 0.81%). These features are likely a result of the high resistivity of the polymer that compromise the electron extraction and promotes higher charge recombination. Likewise, negligible improvement on the photovoltaic parameters was observed after adding 0.3 wt% of MXenes when compared to the pure PMMA device. On the other hand, an enhanced performance was observed when 1.5 wt% of MXene was added to PMMA. PMMA:MX-1.5% based devices showed increased J_{sc} and V_{oc} values of up to 25.1 mA cm^{-2} and 1.15 V, respectively. The improved V_{oc} infers a decrease in recombination losses leading to an enhancement of extracted charges for the PMMA:MX devices. Furthermore, the PMMA:MX-1.5% based devices showed better FF (76.91 ± 2.27), inferring a reduced series resistance. These values were clearly higher than those obtained for the control device without PMMA (Table 1). The enhanced parameters of the PMMA:MX-1.5% device can be attributed to the higher electrical conductivity of the MXenes. Thus, the 2D material acts as an electron conductor, leading to an efficient injection of electrons to the ETL and compensating the poor electrical conduction of pure PMMA. These improvements contributed to increasing the PCE to 21.30 ± 0.51 (22.1% for the benchmark device), which is approximately 10% higher than the control

Table 1 Photovoltaic parameters of the control, PMMA and PMMA:MX PSCs[a] under sun simulated irradiation (AM 1.5G, 100 mW cm^{-2}). In parentheses: the PSC highest value for each configuration

Device		J_{sc} (mA cm^{-2})	V_{oc} (V)	FF (%)	PCE (%)	HI (%)
Control	Rev	22.92 ± 0.45 (22.9)	1.11 ± 0.01 (1.11)	75.26 ± 4.71 (76.8)	19.16 ± 0.81 (19.9)	0.93 ± 1.62
	Fwd	22.61 ± 0.59 (22.6)	1.11 ± 0.02 (1.10)	75.79 ± 3.84 (77.6)	18.98 ± 0.77 (19.7)	
PMMA	Rev	22.13 ± 1.27 (21.9)	1.08 ± 0.02 (1.07)	74.61 ± 5.21 (79.0)	17.78 ± 0.81 (18.69)	4.26 ± 7.38
	Fwd	21.47 ± 1.65 (21.8)	1.08 ± 0.01 (1.08)	73.21 ± 3.07 (75.9)	17.02 ± 1.37 (17.84)	
PMMA:MX-0.3%	Rev	22.77 ± 0.75 (22.2)	1.10 ± 0.01 (1.12)	73.85 ± 2.65 (76.6)	18.42 ± 0.91 (18.9)	4.26 ± 5.88
	Fwd	22.54 ± 1.19 (22.1)	1.09 ± 0.02 (1.11)	71.90 ± 3.87 (74.1)	17.63 ± 1.29 (18.1)	
PMMA:MX-1.5%	Rev	24.45 ± 0.86 (25.1)	1.13 ± 0,02 (1.11)	76.91 ± 2.27 (79.3)	21.30 ± 0.51 (22.1)	2.10 ± 1.23
	Fwd	24.62 ± 0.67 (25.1)	1.13 ± 0.02 (1.11)	75.20 ± 1.80 (77.7)	20.85 ± 0.42 (21.6)	
PMMA:MX-3%	Rev	22.54 ± 1.05 (23.7)	1.09 ± 0,01 (1.10)	77.05 ± 1.97 (78.3)	19.00± 0.97 (20.45)	3.32 ± 2.08
	Fwd	22.08 ± 1.24 (23.5)	1.09 ± 0.01 (1.10)	76.18 ± 1.47 (77.4)	18.38 ± 1.21 (20.01)	

[a] Results refer to an average of eight perovskite solar cells of each configuration. Applied bias voltage in reverse (Rev) and forward (Fwd) scans.

device (19.16 ± 0.81). However, further increase in MXene content resulted in a decrease of PCE (Table 1). This effect is attributed to the restacking of $Ti_3C_2T_x$ nanosheets, compromising their dispersion throughout the film. The lack of appropriate dispersion of the 2D material has a negative impact on the electrical conductivity and topographical characteristics of the film. This effect is corroborated by the progressive increase in film surface roughness as the MXene concentration increases (Fig. S4(b), ESI†).

External quantum efficiency (EQE) spectra and the integrated current curves of the PSCs are exhibited in Fig. 4(b). The EQE spectra showed the highest value for PMMA:MX-1.5% (79.5%) and the lowest for pure PMMA (73%). The integrated currents for the samples exhibit a similar trend from the *J–V* curves (Table 1) for the PMMA:MX-1.5% (23.5 mA cm^{-2}), Control (21.8 mA cm^{-2}) and PMMA (21.2 mA cm^{-2}) based PSCs.

J–V forward scan curves were also measured (Fig. S6(a)–(e), ESI†). Hysteresis indexes (HI) were calculated from eqn (S1) (ESI†) and are presented in Table 1. The control devices (Fig. S6(a), ESI†) exhibit practically coincident forward and reverse *J–V* curves resulting in a HI index of less than 1%. The PMMA layer negatively affected the HI of PSCs (Table 1). Mixing MXene resulted in a decrease in hysteresis in the passivated PSCs, in which the best HI value is found for PMMA:MX-1.5% (HI = 2.10). The hysteretic phenomenon may involve multiple and complex processes, such as an intrinsic perovskite ferroelectric polarization property, migration of ions and their corresponding vacancies within the perovskite, unbalanced electron and hole extractions due to poor conductivity of the charge transport layers and trap-assisted charge recombination at the surface/boundaries of perovskite or at their interfaces with adjacent charge transport layers.[38,39] Our findings indicate that the high electrical conductivity of MXenes favors electron extraction while avoiding charge accumulation at the PMMA interfaces and charge trapping.

To evaluate the impact of PMMA and PMMA:MX layers, series (R_S) and shunt (R_{SH}) resistances of the PSCs were calculated by the differential resistance (R_{diff}) equation from the dark *J–V* curves as shown in Fig. S7 (ESI†):

$$R_{diff} = \frac{dV}{dI} \quad (1)$$

R_S is obtained from the extrapolation of the saturated part at a high forward bias, whereas R_{SH} is from the saturation regime of the resistance closer to the zero-voltage bias.[40] The respective values of R_S and R_{SH} are summarized in Table 2. The device without PMMA presented a R_S of 18 Ω cm^{-2}. For PMMA passivated, the R_S value increased to 38 Ω cm^{-2}. The series resistance dictates the charge carrier injection and extraction in the devices. Thus, a higher resistance causes efficiency losses,[41] in agreement with the photovoltaic performance found in Table 1. The presence of MXenes resulted in a progressive decrease of R_S reaching 15 Ω cm^{-2} for PMMA:MX-3%, as expected. This trend could be mainly attributed to the high electrical conductivity of the $Ti_3C_2T_x$. On the other hand, devices without PMMA showed the lowest R_{SH} of 3.9×10^4 Ω, which increased about two orders of magnitude when PMMA is introduced. The shunt resistance is manly related to ''leakage currents'' within the device materials and architecture. The increase in shunt resistance is related to the suppression in leakage current, or a reduction in current recombination and consequently an improvement in FF and the overall PSC performance.[41] Although MXene mixing in PMMA induces a slight decrease in shunt resistance (R_{SH} = 6.7×10^5 for PMMA:MX-3%), they are still higher than the control device, as shown in Table 2.

Table 2 Device series resistance (R_S), shunt resistance (R_{SH}), ideality factor (n), power parameter of J_{sc} light dependent measurement (α) and trap density parameters (N_t and $N_{t,IS}$) of the control, PMMA and PMMA:MX (0.3, 1.5 and 3.0 wt%)

Device	R_S (Ω)	R_{SH} (Ω)	n	α	N_t (cm^{-3})	N_{tIS} (eV^{-1} cm^{-3})
Control	18	3.9×10^4	1.91	0.977	7.03×10^{17}	7.2×10^{17}
PMMA	38	3.9×10^6	2.95	0.863	3.08×10^{17}	1.5×10^{17}
PMMA:MX-0.3%	31	1.2×10^6	1.66	0.949	3.56×10^{17}	2.9×10^{17}
PMMA:MX-1.5%	18	9.9×10^5	1.67	0.985	4.15×10^{17}	4.5×10^{17}
PMMA:MX-3.0%	15	6.7×10^5	1.88	0.980	5.33×10^{17}	5.8×10^{17}

To study the phenomena involving the enhancement of performance of PMMA:MX based devices, we performed different opto-electronic characterizations. An interesting approach to investigate recombination kinetics on perovskite solar cells is to evaluate J_{sc} and V_{oc} under different light intensities. Fig. 4(c) shows the measured V_{oc} at various sunlight intensities. Under open-circuit conditions, the recombination behavior can be related to V_{oc} by the equation below:

$$V_{OC} = \frac{nkT}{q} \ln I \quad (2)$$

where n is the ideality factor of the device, k is the Boltzmann constant, T is the temperature, q is the elementary charge and I is the light intensity.[42] Overall, the ideality factor (n) can be used to infer the dominant recombination in PSCs. n = 1 is attributed to second-order (bimolecular) charge-carrier radiative recombination, while n = 2 to a first-order (monomolecular) trap-assisted non-radiative recombination.[43] The calculated values of n for all devices are summarized in Table 2. Generally, charge recombination of PSCs under light results from a trade-off between trap-related monomolecular and bimolecular electron–hole recombination.[44] The ideality factor of the control devices suggests a dominance of trap-assisted monomolecular recombination, whereas PMMA:MX passivated non-radiative recombination.[45] Thus, the decrease in non-radiative recombination after the introduction of MXenes was reflected in the enhancement of V_{oc} for PMMA:MX based devices, as shown in Table 1. n exceeding 2 for the PMMA device may be related to tail states[46] and transport losses[47] due to the high resistivity of the polymer and consequent reduced charge transport. Similar behavior was observed by Wang *et al.*[13] after incorporation of PMMA in n–i–p PSCs, attributing $n > 2$ to recombination losses. Fig. 4(d) shows the measured J_{sc} as a function of light intensity. J_{sc} can be approximated to I^{α}, where I is the light

intensity. When α = 1, all carriers are extracted without recombination.[48] The calculated values of α for all devices are summarized in Table 2. Likewise, the calculated α value for pure PMMA devices (0.863) indicates an increase in recombination, which is mitigated by MXenes (α = 0.985).

Recombination was also studied using the transient photovoltage (TPV). In this experiment, a 200 μs light pulse is applied in the device under open circuit conditions. After switching off the light, the V_{oc} profile was collected. Since during measurements no charge is extracted, the transient V_{oc} decay is assigned to the recombination processes of the photo generated carriers. All TPV curves (Fig. S8(a), ESI†) could be fitted by a biexponential decay (eqn (S2), ESI†) and the results are summarized in Table S2 (ESI†). For PSCs, typically two characteristic decay lifetimes are extracted: a shorter time constant (τ_1) that spans microseconds, assigned to nonradiative recombination at the surfaces and interfaces between perovskite/charge transport layers; and a longer time constant (τ_2) related to recombination in the bulk of the perovskite layer.[49–51] Table S2 (ESI†) also shows the average lifetime (τ) according to eqn (S3) (ESI†). The use of a pure PMMA layer resulted in a slight decrease of both fast and slow charge-carrier lifetimes contributing to a reduction of τ to 0.53 ms when compared to the control devices (0.88 ms). On the other hand the optimal concentration of MXenes (1.5 wt%) resulted in an enhancement in the average charge-carrier lifetime (τ = 0.92 ms) implying a recombination mitigation. These results are in agreement with the faster extraction times (t_e) for PMMA:MX obtained from the transient photocurrent (TPC) analysis (Fig. S8(b), ESI†). The TPC curves were fitted according to eqn (S4) (ESI†) and t_e values are shown in Table S2 (ESI†). The introduction of MXene results in gradual reduction of t_e reaching 1.24 μs (1.5 wt%) against 1.47 μs for the control device.

Steady PL and TRPL spectra were measured to evaluate the charge extraction dynamics from perovskite/PMMA:MX/PCBM interfaces. Interestingly, mixing of MXenes into PMMA resulted in a gradual quenching of the PL intensity, inferring an efficient carrier extraction process from perovskite to the PCBM layer[52] (Fig. 4(e)). These results were corroborated by TRPL measurements (Fig. 4(f)). The TRPL spectra could be fitted by a biexponential decay (eqn (S2) and (S3), ESI†) and the results are summarized in Table S3 (ESI†). The addition of pure PMMA and PMMA:MX showed a decrease in average carrier extraction lifetimes to 52.0 and 58.5 ns, respectively, when compared to the control devices (108.5 ns). These results show the addition of the PMMA:MX passivation layer facilitates charge extraction from perovskite to PCBM,[53,54] which is consistent with TPC analysis.

In addition, the recombination losses of the passivated devices were studied using trap-filled-limited voltage (V_{TFL}) obtained from the log–log J–V curves under dark conditions (Fig. S9, ESI†). The trap density (N_t) was calculated according to eqn (3):

$$V_{TFL} = \frac{qN_tL^2}{2\varepsilon\varepsilon_o} \quad (3)$$

where q is the elementary charge, L is the perovskite thickness, ε is the dielectric constant, and ε_o is the vacuum permittivity.[55] The dielectric constant was evaluated from the capacitance of our devices ($C_g = \frac{\varepsilon_0\varepsilon}{L}$) and estimated as $\varepsilon \sim 21$.[56] As shown on Fig. S10 (ESI†), the geometric capacitance (C_g) was extracted from the capacitance–voltage measurements in the dark of the control device at negative bias and 100 kHz. The values of N_t are summarized in Table 2. Interestingly, the control devices presented the highest N_t (7.03×10^{17} cm^{-3}), which decreased to 3.08×10^{17} cm^{-3} when the PMMA passivation layer is used. These results indicate that the polymer layer passivates trap sites in the devices. Surprisingly, the added MXene into PMMA resulted in a slight increase in N_t to 5.33×10^{17} cm^{-3} (PMMA:MX-3.0%), which is still smaller than the control devices. It is known that monomolecular (nonradiative recombination) processes are mainly mediated by defects in the perovskite bulk or interfaces between the perovskite and charge transport layers. At the former, the presence of traps is mainly due to grain boundaries and elemental vacancies, interstitials or substitutions from the crystalline perovskite.[57] Interface induced recombination is mainly governed by defects, as well as mismatched energy-level alignment and charge-carrier back transfer.[58] As shown by the AFM analysis, the large contents of MXene slightly increased the RMS of the passivation layers thus enhancing charge accumulation sites at the perovskite/ETL interface. These results are in line with the slight increase of N_t for PMMA:MX when compared to PMMA (Table 2). On the other hand, the presence of the $Ti_3C_2T_x$ improves the electrical conductivity of the PMMA based passivation layer as well as its wettability characteristics. The passivation effect of PMMA:MX is then a result of the optimal combination of the interfacial features. Therefore, the N_t reduction after PMMA and PMMA-MX layer deposition shows that interface defects are being passivated, as expected.

To gain a deeper insight into the dynamics of the photogenerated charge carriers, the linearly increasing voltage (photo-CELIV) was measured. For this technique, charge carriers were photo-generated in the devices using a 100 μs light pulse illumination. Immediately after ceasing illumination, charge extraction was performed by a bias voltage under different ramp rates. The charge mobility (μ) was calculated using eqn (4), proposed by Lorrmann *et al*:[59]

$$\mu = \frac{d^2}{2At_{max^2}}\left[\frac{1}{6.2\left(1+0.002\frac{\Delta j}{j_0}\right)} + \frac{1}{\left(1+0.12\frac{\Delta j}{j_0}\right)}\right]^2 \quad (4)$$

where d is the device thickness, A refers to the applied voltage ramp, t_{max} corresponds to the time at current maxima and Δj is the current increment from the dark-CELIV curve (j_0). Fig. 5(a) and Fig. S11 (ESI†) show the typical photo-CELIV transients and Δj curves for the PSCs with the peak position relating to the charge mobility. Fig. 5(b) shows the calculated μ for the PSCs according to Δj curves. PMMA passivated PSC showed t_{max} at longer time, indicating that a longer period was needed for maximum extraction of charge carriers. This result was reflected in the decreased μ when compared to the control PSC. For instance, at a voltage ramp of 50 k V s^{-1}, μ reduced

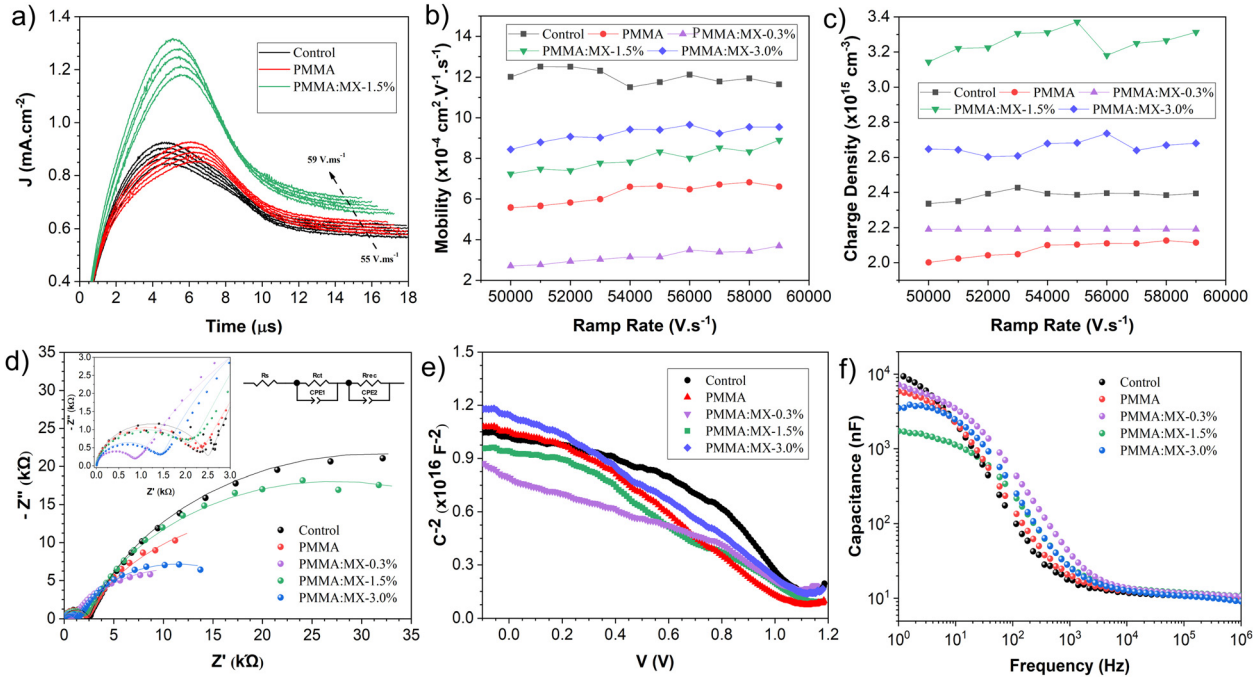

Fig. 5 (a) Photo-CELIV transients at varying ramp rates; (b) charge mobility and (c) extracted charge carrier density obtained from photo-CELIV transients. (d) Nyquist plots (symbols) and fitting curves (lines) of the devices under illumination. (e) Mott–Schottky plots from the capacitance behavior in the dark. (f) Capacitance *vs.* frequency curves carried out under illumination. The IS measurements were measured at 0 V bias.

from 11.90×10^{-4} cm^2 V^{-1} s^{-1} (Control) to 5.5×10^{-4} cm^2 V^{-1} s^{-1} (PMMA passivated device). Even though mixing MXene resulted in a μ increase, 8.4×10^{-4} cm^2 V^{-1} s^{-1} for PMMA:MX 10%, it is still worse compared to the control device. On the other hand, a substantial enhancement in the density of extracted charge carriers (n_c) is observed after the addition of MXene. The n_c values were calculated by integrating the photo-CELIV transients and are shown in Fig. 5(c). The use of pure PMMA negatively affected n_c leading to a considerable decrease in extracted carrier when compared to the control device. The increased concentration of MXene on the contrary led to an enhancement in n_c (Fig. 5(c)). The best n_c was achieved for PMMA:MX-1.5%, and was about 40% larger than the control device.

The charge mobility and number of extracted charges are strongly affected by several phenomena including trap-detrapping events associated with surface and interface defects.[60,61] Even though the presence of PMMA resulted in enhanced ETL film formation with reduced interfacial defects, the low conductivity of PMMA compromised the electron mobility and extraction. The metallic characteristic of $Ti_3C_2T_x$ otherwise provides a free-path for the electron transport, favoring the charge migration to the ETL. However, the large content of MXenes may result in agglomeration of the 2D materials, promoting a depreciation of surface features (higher roughness) and compromising charge extraction. Therefore, the optimal concentration of MXene into the PMMA layer depends on a trade-off between high conductivity and appropriate film interfacial features.

Nyquist plots measured under illumination and at 0 V are shown in Fig. 5(d). The data were fitted using the equivalent circuit in Fig. 5(d), used to extract the charge transport (R_{ct}) and recombination (R_{rec}) resistances.[62] R_{ct} was reduced with the MXene inferring a better charge transfer through the metallic MXene based devices (Table S3, ESI†). The presence of the polymeric layer otherwise resulted in a reduction of R_{rec} due to more recombination events at PMMA based PSCs. Interestingly, R_{rec} is increased for PMMA:MX-1.5% (Table S3, ESI†). The low R_{ct} and high R_{rec} suggests a more efficient extraction of charges in addition to the suppression of charge recombination for the PMMA:MX-1.5%, which is in agreement with the enhanced photovoltaic performance shown in Table 1.

The PMMA:MX-1.5% showed an overall higher V_{oc} compared to the other devices (Table 1). The Mott–Schottky analysis was used to understand the origin of the difference in this parameter. For reliable data acquisition of the depletion layer capacitance, the capacitance–voltage was measured in the dark at three frequencies that lie in the dielectric response range (10, 55 and 100 kHz), as shown in Fig. S12(a) (ESI†). We chose 100 kHz to avoid low-frequency influences.[63] Fig. S12(b) (ESI†) shows the capacitance–voltage spectra for the control, PMMA and PMMA:MX devices, which were used to produce Fig. 5(e). The built-in potential (V_{bi}) was calculated using the following equation:[56]

$$C_{dl}^{-2} = \frac{2}{q\varepsilon\varepsilon_0 N}(V_{bi} - V) \quad (5)$$

where C_{dl} is the depletion layer capacitance and N is the charge density. The PMMA passivation layer reduced V_{bi} in 50 mV when compared to the control device (1.14 to 1.09 V). MXenes increased V_{bi} for PMMA:MX-1.5% (V_{bi} = 1.21 V).

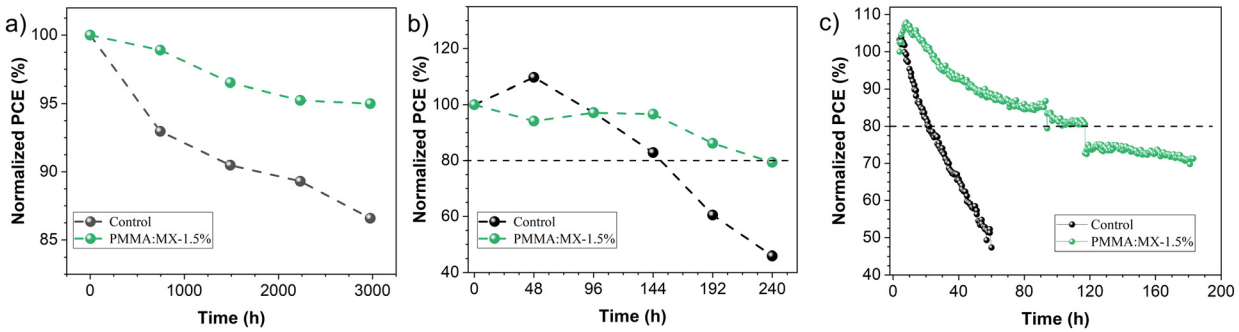

Fig. 6 Normalized PCE over time for the control and PMMA:MX-1.5% devices: (a) ISOS-D-1I, (b) ISOS-D-1 and (c) ISOS-L-2 stability tests.

Recent literature shows that the frequency dependence of capacitance (C–f) under illumination in PSCs has distinct regimes due to the charge dynamics in the device.[64] At high-frequencies, a plateau can be observed due to the intrinsic dielectric polarization of the bulk perovskite (C_{bulk}),[65] whereas in the low-frequency region slow mechanisms including ionic/electronic interface processes are dominant.[66,67] Based on Fig. 5(f), all devices showed similar C_{bulk}, in agreement that the perovskite layer is similar in all devices. However, a clear distinction is observed at low frequencies. PMMA produced the highest capacitance, which indicates an increased accumulation of carriers at the perovskite/ETL interface, corroborating the poor charge extraction and mobility characteristics shown from CELIV (Fig. 5(a)–(c)). On the other hand, the PMMA:MX reduced the capacitance due to the favored electron extraction.

C–f under dark conditions is provided in Fig. S12(a) (ESI†) as additional evidence for the reduction of the trap states in our devices. The defect density (N_{tIS}) can be determined from the capacitance $C(\omega)$ derivative (Fig. S12(b), ESI†) as follows:[68]

$$N_{t,IS} = -\frac{V_{bi}\omega}{qLk_bT}\frac{dC(\omega)}{d\omega} \quad (6)$$

where L is the absorber layer thickness, V_{bi} is the built-in potential, and ω is the applied angular frequency. Fig. S12(c) (ESI†) shows that the passivation layers reduced the N_{tIS} (*i.e.* 4.5×10^{17} eV^{-1} cm^{-3} for the PMMA:MX-1.5%) compared to the control device (7.2×10^{17} eV^{-1} cm^{-3}). The values of the N_{tIS} taken from the low frequency are shown in Table 2. This finding agrees with the values obtained from V_{tfl} indicating a reduction of deep-level traps.[69]

Table S3 (ESI†) summarizes the impedance spectroscopy results. PMMA:MX-1.5% based PSCs presented a low R_{ct} and the highest R_{rec} among the passivated devices, in addition to the highest V_{bi}, and the reduced N_{tIS}. These values corroborate the higher charge mobility, better extracted photocurrent, and lower recombination for the PMMA:MX-1.5% device than the control.

PSC stability tests

A critical issue for PSC technology is their stability, which is very sensitive to intrinsic (ion migration, defect concentration) and extrinsic (oxygen moisture, heat, light) factors. We monitored the PSC degradation stored under an inert atmosphere (ISOS-D-1I), as shown in Fig. 6(a). PMMA:MX-1.5% showed enhanced device stability retaining about 95% of its initial PCE after 3000 h, against 86% of the control device. These results can be attributed to the defect passivation effect of the PMMA:MX layer.[70] The PMMA:MX passivation layer produced PCBM films of better quality, due to the nonpolar nature of the solvent CB. Moreover, both PMMA and MXene possess oxygen functional groups which may work as a Lewis base interacting with under-coordinated cations from the perovskite. Finally, the passivation layer works as a physical barrier for ion migration from and to the perovskite layers avoiding the formation of deleterious phases such as AgI or AgBr.

The hydrophobic nature and physical barrier of the passivation layer mitigated the degradation induced by moisture and oxygen. Fig. 6(b) shows that the devices with PMMA:MX lasted 100 h longer than the control devices under ISOS-D-1 tests. Several phenomena like ion-migration, phase segregation and defect generation are strongly influenced or increased by light.[71,72] To evaluate the effect of light and heat on the PSCs, we monitored encapsulated PSCs under the ISOS-L-2 protocol (Fig. 6(c)). Under this protocol, PMMA-MX-1.5% PSCs lasted three times longer than the control device. Therefore, the stability tests suggest that the MXene mixed with PMMA enhance the device's performance and stability.

Conclusions

$Ti_3C_2T_x$ MXene was successfully incorporated into PMMA as a passivation layer in inverted PSCs. The PMMA:MX passivation layer provided a good interfacial layer between the perovskite and the ETL resulting in better photovoltaic parameters. PMMA:MX-1.5% PSC had the highest J_{sc} (24.45 ± 0.86 mA cm^{-2}) and FF ($76.91 \pm 2.27\%$) due to a better electron extraction. The V_{oc} was improved to values up to 1.15 V inferring a decrease in recombination in the devices with the PMMA:MX layer. These values contributed to boosting the PCE of PSCs to $21.30 \pm 0.51\%$ (22.1% for the benchmark PSC). The $Ti_3C_2T_x$ mixed in PMMA favors electron migration to the ETL, decreasing recombination, as shown by PL and TPV spectroscopies. The reduced recombination is also reflected in the fast extraction time and a higher density of extracted charges for PMMA:MX by TRPL, TPC, and photo-CELIV,

respectively. Impedance spectroscopy showed that the low R_{ct} and high R_{rec}, in addition to the highest V_{bi} and the reduced N_{tIS} are found for PMMA:MX-1.5%. Solar cells with PMMA:MX also showed better stability retaining 95% of its original PCE after 3000 h (ISOS-D-1I) and lasting three times longer compared to the control PSC under light soaking and heat (ISOS-L-2). Future approaches should focus on other 2D materials from the class of MXenes as additives for thin polymer passivation films.

Author contributions

J. P. F. A. started the work, fabricated the PSCs devices, carried out electrical measurements and analyzed data; H. G. L. and J. H. H. R. conceived the work; wrote and edited the manuscript with input from all authors. J. V. M. L. synthesized MXene; performed XRD and UV-vis. G. L. N. performed AFM and EIS measurements and analyzed data. S. L. F. and D. B. carried out EQE measurements. R. V. F. and S. A. L. carried out PL and TRPL measurements. R. K. N. and S. F. S. carried out FE-SEM imaging. C. F. O. G. supervised the work and provided funding. All authors reviewed the manuscript.

Conflicts of interest

There are no conflicts to declare.

Acknowledgements

The authors gratefully acknowledge the financial support of FAPESP (grants: 20/12356-8, 13/07296-2, 20/16470-0, 22/10998-8, 20/15632-6, 21/03379-7, 19/22183-6), Centro de Desenvolvimento de Materiais Funcionais – CDMF, FINEP (grant: 01.22.0289.00 (0034/21)), UNESP (grant: 4224) and CAPES. The authors also acknowledge MSc. Gabriela Amorim and Maria L. Viela from Oninn for the contact angle measurements and stability tests (ISOS-L2) and Prof. Dr Valmor Mastelaro for XPS measurements. S. F. Santos acknowledges CNPq (grant: 2020/310984-3). The authors are grateful to the Multiuser Central Facilities (UFABC) for the support with the FE-SEM analysis.

References

1 P. Roy, N. Kumar Sinha, S. Tiwari and A. Khare, *Sol. Energy*, 2020, **198**, 665–688.
2 Y. Bai, X. Meng and S. Yang, *Adv. Energy Mater.*, 2018, **8**, 1–14.
3 X. Lin, D. Cui, X. Luo, C. Zhang, Q. Han, Y. Wang and L. Han, *Energy Environ. Sci.*, 2020, **13**, 3823–3847.
4 M. H. Miah, M. B. Rahman, M. Nur-E-Alam, N. Das, N. B. Soin, S. F. W. M. Hatta and M. A. Islam, *ChemNanoMat*, 2023, **8**(3), e202200471.
5 Z. Li, C. Xiao, Y. Yang, S. P. Harvey, D. H. Kim, J. A. Christians, M. Yang, P. Schulz, S. U. Nanayakkara, C. S. Jiang, J. M. Luther, J. J. Berry, M. C. Beard, M. M. Al-Jassim and K. Zhu, *Energy Environ. Sci.*, 2017, **10**, 1234–1242.
6 D. Y. Heo, W. J. Jang and S. Y. Kim, *Mater. Today Chem.*, 2022, **26**, 101224.
7 F. Yang, H. E. Lim, F. Wang, M. Ozaki, A. Shimazaki, J. Liu, N. B. Mohamed, K. Shinokita, Y. Miyauchi, A. Wakamiya, Y. Murata and K. Matsuda, *Adv. Mater. Interfaces*, 2018, **5**, 1–10.
8 S. Zhang, M. Li, H. Zeng, X. Zheng, L. Luo, S. You, Y. Zhao, R. Liu, C. Tian and X. Li, *ACS Energy Lett.*, 2022, **7**, 3958–3966.
9 F. Wu, Z. Luo, L. Zhu, C. Chen, H. Lu, Z. Chen, J. Tang and C. Yang, *J. Mater. Chem. A*, 2019, **7**, 21176–21181.
10 K. Liu, S. Dai, F. Meng, J. Shi, Y. Li, J. Wu, Q. Meng and X. Zhan, *J. Mater. Chem. A*, 2017, **5**, 21414–21421.
11 R. Wang, J. Qiao, B. He, X. Tang, F. Wu and L. Zhu, *J. Mater. Chem. C*, 2018, **6**, 8429–8434.
12 Q. Wang, Q. Dong, T. Li, A. Gruverman and J. Huang, *Adv. Mater.*, 2016, **28**, 6734–6739.
13 F. Wang, A. Shimazaki, F. Yang, K. Kanahashi, K. Matsuki, Y. Miyauchi, T. Takenobu, A. Wakamiya, Y. Murata and K. Matsuda, *J. Phys. Chem. C*, 2017, **121**, 1562–1568.
14 J. Peng, J. I. Khan, W. Liu, E. Ugur, T. Duong, Y. Wu, H. Shen, K. Wang, H. Dang, E. Aydin, X. Yang, Y. Wan, K. J. Weber, K. R. Catchpole, F. Laquai, S. De Wolf and T. P. White, *Adv. Energy Mater.*, 2018, **8**, 1–9.
15 F. Zhang, J. Song, R. Hu, Y. Xiang, J. He, Y. Hao, J. Lian, B. Zhang, P. Zeng and J. Qu, *Small*, 2018, **14**, 1704007.
16 P. Ferdowsi, E. Ochoa-Martinez, S. S. Alonso, U. Steiner and M. Saliba, *Sci. Rep.*, 2020, **10**, 1–10.
17 X. Hu, H. Wang, M. Wang and Z. Zang, *Sol. Energy*, 2020, **206**, 816–825.
18 J. Peng, Y. Wu, W. Ye, D. A. Jacobs, H. Shen, X. Fu, Y. Wan, T. Duong, N. Wu, C. Barugkin, H. T. Nguyen, D. Zhong, J. Li, T. Lu, Y. Liu, M. N. Lockrey, K. J. Weber, K. R. Catchpole and T. P. White, *Energy Environ. Sci.*, 2017, **10**, 1792–1800.
19 R. M. Ronchi, J. T. Arantes and S. F. Santos, *Ceram. Int.*, 2019, **45**, 18167–18188.
20 T. Schultz, N. C. Frey, K. Hantanasirisakul, S. Park, S. J. May, V. B. Shenoy, Y. Gogotsi and N. Koch, *Chem. Mater.*, 2019, **31**, 6590–6597.
21 J. L. Hart, K. Hantanasirisakul, A. C. Lang, B. Anasori, D. Pinto, Y. Pivak, J. T. van Omme, S. J. May, Y. Gogotsi and M. L. Taheri, *Nat. Commun.*, 2019, **10**(522), 1–10.
22 Z. Yu, W. Feng, W. Lu, B. Li, H. Yao, K. Zeng and J. Ouyang, *J. Mater. Chem. A*, 2019, **7**, 11160–11169.
23 H. G. Lemos, R. M. Ronchi, G. R. Portugal, J. H. H. Rossato, G. S. Selopal, D. Barba, E. C. Venancio, F. Rosei, J. T. Arantes and S. F. Santos, *ACS Appl. Energy Mater.*, 2022, **5**(12), 15928–15938.
24 S. Qamar, K. Fatima, N. Ullah, Z. Akhter, A. Waseem and M. Sultan, *Nanoscale*, 2022, **14**, 13018–13039.
25 D. Saranin, S. Pescetelli, A. Pazniak, D. Rossi, A. Liedl, A. Yakusheva, L. Luchnikov, D. Podgorny, P. Gostischev, S. Didenko, A. Tameev, D. Lizzit, M. Angelucci, R. Cimino, R. Larciprete, A. Agresti and A. Di Carlo, *Nano Energy*, 2021, **82**, 105771.
26 A. Di Vito, A. Pecchia, M. Auf der Maur and A. Di Carlos, *Adv. Funct. Mater.*, 2020, **30**, 1909028.

27 H. G. Lemos, J. H. H. Rossato, R. A. Ramos, J. V. M. Lima, L. J. Affonço, S. Trofimov, J. J. I. Michel, S. L. Fernandes, B. Naydenov and C. F. O. Graeff, *J. Mater. Chem. C*, 2023, 3571–3580.

28 J. Zhang, C. Huang, Y. Sun and H. Yu, *Adv. Funct. Mater.*, 2022, **32**, 1–14.

29 A. Yakusheva, D. Saranin, D. Muratov, P. Gostishchev, H. Pazniak, A. Di Vito, T. S. Le, L. Luchnikov, A. Vasiliev, D. Podgorny, D. Kuznetsov, S. Didenko and A. Di Carlo, *Small*, 2022, **18**(37), 2201730.

30 V. S. N. Chava, P. S. Chandrasekhar, A. Gomez, L. Echegoyen and S. T. Sreenivasan, *ACS Appl. Energy Mater.*, 2021, **4**, 12137–12148.

31 R. M. Ronchi, S. F. Santos and R. G. A. Veiga, *Appl. Surf. Sci.*, 2023, **609**, 155344.

32 M. Alhabeb, K. Maleski, B. Anasori, P. Lelyukh, L. Clark, S. Sin and Y. Gogotsi, *Chem. Mater.*, 2017, **29**, 7633–7644.

33 M. V. Khenkin, E. A. Katz, A. Abate, G. Bardizza, J. J. Berry, C. Brabec, F. Brunetti, V. Bulović, Q. Burlingame, A. Di Carlo, R. Cheacharoen, Y. B. Cheng, A. Colsmann, S. Cros, K. Domanski, M. Dusza, C. J. Fell, S. R. Forrest, Y. Galagan, D. Di Girolamo, M. Grätzel, A. Hagfeldt, E. von Hauff, H. Hoppe, J. Kettle, H. Köbler, M. S. Leite, S. (Frank) Liu, Y. L. Loo, J. M. Luther, C. Q. Ma, M. Madsen, M. Manceau, M. Matheron, M. McGehee, R. Meitzner, M. K. Nazeeruddin, A. F. Nogueira, Ç. Odabaşı, A. Osherov, N. G. Park, M. O. Reese, F. De Rossi, M. Saliba, U. S. Schubert, H. J. Snaith, S. D. Stranks, W. Tress, P. A. Troshin, V. Turkovic, S. Veenstra, I. Visoly-Fisher, A. Walsh, T. Watson, H. Xie, R. Yıldırım, S. M. Zakeeruddin, K. Zhu and M. Lira-Cantu, *Nat. Energy*, 2020, **5**, 35–49.

34 K. Maleski, C. E. Shuck, A. T. Fafarman and Y. Gogotsi, *Adv. Opt. Mater.*, 2021, **9**, 2001563.

35 E. Colin-Ulloa, A. Fitzgerald, K. Montazeri, J. Mann, V. Natu, K. Ngo, J. Uzarski, M. W. Barsoum and L. V. Titova, *Adv. Mater.*, 2023, **35**, 2208659.

36 Q. Zhou, L. Liang, J. Hu, B. Cao, L. Yang, T. Wu, X. Li, B. Zhang and P. Gao, *Adv. Energy Mater.*, 2019, **9**, 1802595.

37 A. Tong, C. Zhu, H. Yan, C. Zhang, Y. Jin, Y. Wu, F. Cao, J. Wu and W. Sun, *J. Alloys Compd.*, 2023, **942**, 169084.

38 P. Liu, W. Wang, S. Liu, H. Yang and Z. Shao, *Adv. Energy Mater.*, 2019, **9**, 1803017.

39 B. Chen, M. Yang, S. Priya and K. Zhu, *J. Phys. Chem. Lett.*, 2016, **7**, 905–917.

40 V. V. Brus, F. Lang, J. Bundesmann, S. Seidel, A. Denker, B. Rech, G. Landi, H. C. Neitzert, J. Rappich and N. H. Nickel, *Adv. Electron. Mater.*, 2017, **3**(2), 1600438.

41 K. Tvingstedt, L. Gil-Escrig, C. Momblona, P. Rieder, D. Kiermasch, M. Sessolo, A. Baumann, H. J. Bolink and V. Dyakonov, *ACS Energy Lett.*, 2017, **2**, 424–430.

42 R. D. Chavan, N. Parikh, M. M. Tavakoli, D. Prochowicz, A. Kalam, P. Yadav, P. H. Bhoite and C. K. Hong, *Adv. Mater. Interfaces*, 2021, **8**, 2100177.

43 P. Caprioglio, C. M. Wolff, O. J. Sandberg, A. Armin, B. Rech, S. Albrecht, D. Neher and M. Stolterfoht, *Adv. Energy Mater.*, 2020, **10**, 1–9.

44 C. L. Davies, M. R. Filip, J. B. Patel, T. W. Crothers, C. Verdi, A. D. Wright, R. L. Milot, F. Giustino, M. B. Johnston and L. M. Herz, *Nat. Commun.*, 2018, **9**, 1–9.

45 K. J. Rietwyk, X. Lin, B. Tan, T. Warnakula, P. Holzhey, B. Zhao, S. Deng, M. A. Surmiak, J. Jasieniak and U. Bach, *Adv. Energy Mater.*, 2023, **13**, 2200796.

46 T. Kirchartz, B. E. Pieters, J. Kirkpatrick, U. Rau and J. Nelson, *Phys. Rev. B: Condens. Matter Mater. Phys.*, 2011, **83**, 115209.

47 W. Tress, M. Yavari, K. Domanski, P. Yadav, B. Niesen, J. P. Correa Baena, A. Hagfeldt and M. Graetzel, *Energy Environ. Sci.*, 2018, **11**, 151–165.

48 Y.-M. M. Sung, A. K. Akbar, S. Biring, C.-F. F. Li, Y.-C. C. Huang and S.-W. W. Liu, *J. Mater. Chem. C*, 2021, **9**, 1196–1204.

49 I. Ka, I. M. Asuo, R. Nechache and F. Rosei, *Chem. Eng. J.*, 2021, **423**, 130334.

50 F. Zhang, Z. Wang, H. Zhu, N. Pellet, J. Luo, C. Yi, X. Liu, H. Liu, S. Wang, X. Li, Y. Xiao, S. M. Zakeeruddin, D. Bi and M. Grätzel, *Nano Energy*, 2017, **41**, 469–475.

51 D. Shi, V. Adinolfi, R. Comin, M. Yuan, E. Alarousu, A. Buin, Y. Chen, S. Hoogland, A. Rothenberger, K. Katsiev, Y. Losovyj, X. Zhang, P. A. Dowben, O. F. Mohammed, E. H. Sargent and O. M. Bakr, *Science*, 2015, **347**, 519–522.

52 L. Zhou, J. Chang, Z. Liu, X. Sun, Z. Lin, D. Chen, C. Zhang, J. Zhang and Y. Hao, *Nanoscale*, 2018, **10**, 3053–3059.

53 W. Wang, Z. Yang, J. Ding, J. Kong and X. Li, *Sol. Energy Mater. Sol. Cells*, 2022, **238**, 111609.

54 Z. Wang, P. Fan, D. Zhang, G. Yang and J. Yu, *Synth. Met.*, 2020, **265**, 116428.

55 V. M. Le Corre, E. A. Duijnstee, O. El Tambouli, J. M. Ball, H. J. Snaith, J. Lim and L. J. A. Koster, *ACS Energy Lett.*, 2021, **6**, 1087–1094.

56 O. Almora, C. Aranda, E. Mas-Marzá and G. Garcia-Belmonte, *Appl. Phys. Lett.*, 2016, **109**(17), 173903.

57 W. J. Yin, T. Shi and Y. Yan, *Appl. Phys. Lett.*, 2014, **104**(6), 063903.

58 D. Luo, R. Su, W. Zhang, Q. Gong and R. Zhu, *Nat. Rev. Mater.*, 2019, **5**, 44–60.

59 J. Lorrmann, B. H. Badada, O. Inganäs, V. Dyakonov and C. Deibel, *J. Appl. Phys.*, 2010, **108**, 113705.

60 H. Jin, E. Debroye, M. Keshavarz, I. G. Scheblykin, M. B. J. Roeffaers, J. Hofkens and J. A. Steele, *Mater. Horiz.*, 2020, **7**, 397–410.

61 F. Gao, Y. Zhao, X. Zhang and J. You, *Adv. Energy Mater.*, 2020, **10**, 1902650.

62 L. Yang, F. Cai, Y. Yan, J. Li, D. Liu, A. J. Pearson and T. Wang, *Adv. Funct. Mater.*, 2017, **27**, 1702613.

63 J.-Y. Seo, H.-S. Kim, S. Akin, M. Stojanovic, E. Simon, M. Fleischer, A. Hagfeldt, S. M. Zakeeruddin and M. Grätzel, *Energy Environ. Sci.*, 2018, **11**, 2985–2992.

64 D. A. Jacobs, H. Shen, F. Pfeffer, J. Peng, T. P. White, F. J. Beck and K. R. Catchpole, *J. Appl. Phys.*, 2018, **124**(22), 225702.

65 A. Guerrero, G. Garcia-Belmonte, I. Mora-Sero, J. Bisquert, Y. S. Kang, T. J. Jacobsson, J.-P. Correa-Baena and A. Hagfeldt, *J. Phys. Chem. C*, 2016, **120**, 8023–8032.

66 O. Almora, I. Zarazua, E. Mas-Marza, I. Mora-Sero, J. Bisquert and G. Garcia-Belmonte, *J. Phys. Chem. Lett.*, 2015, **6**, 1645–1652.

67 P. Lopez-Varo, J. A. Jiménez-Tejada, M. García-Rosell, S. Ravishankar, G. Garcia-Belmonte, J. Bisquert and O. Almora, *Adv. Energy Mater.*, 2018, **8**, 1–36.
68 O. Almora, M. García-Batlle and G. Garcia-Belmonte, *J. Phys. Chem. Lett.*, 2019, **10**, 3661–3669.
69 T. Majhi, M. Sridevi, S. Jain, A. Srivastava, M. Kumar, S. K. Srivastava and R. K. Singh, *ACS Appl. Energy Mater.*, 2023, **6**, 8695–8706.
70 A. K. Jena, A. Kulkarni and T. Miyasaka, *Chem. Rev.*, 2019, **119**, 3036–3103.
71 C. G. Bischak, C. L. Hetherington, H. Wu, S. Aloni, D. F. Ogletree, D. T. Limmer and N. S. Ginsberg, *Nano Lett.*, 2017, **17**, 1028–1033.
72 Y. Luo, P. Khoram, S. Brittman, Z. Zhu, B. Lai, S. P. Ong, E. C. Garnett and D. P. Fenning, *Adv. Mater.*, 2017, **29**, 1703451.

